Reporting of quantitative oxygen mapping in EPR imaging

Sankaran Subramanian [a,1], Nallathamby Devasahayam [a,1], Alan McMillan [b], Shingo Matsumoto [a], Jeeva P. Munasinghe [c], Keita Saito [a], James B. Mitchell [a], Gadisetti V.R. Chandramouli [d], Murali C. Krishna [a,*]

[a] Radiation Biology Branch, Center for Cancer Research, National Cancer Institute, NIH, Bethesda, MD 20892, USA
[b] Department of Diagnostic Radiology and Nuclear Medicine, University of Maryland School of Medicine, Baltimore, MD 21201, USA
[c] National Institute of Neurological Disorders and Stroke, NIH, Bethesda, MD 20892, USA
[d] GenEpria Consulting Inc., 10015 Old Columbia Rd., Suite B-215, Columbia, MD 21046, USA

ARTICLE INFO

ABSTRACT

Oxygen maps derived from electron paramagnetic resonance spectral–spatial imaging (EPRI) are based upon the relaxivity of molecular oxygen with paramagnetic spin probes. This technique can be combined with MRI to facilitate mapping of pO_2 values in specific anatomic locations with high precision. The co-registration procedure, which matches the physical and digital dimensions of EPR and MR images, may present the pO_2 map at the higher MRI resolution, exaggerating the spatial resolution of oxygen, making it difficult to precisely distinguish hypoxic regions from normoxic regions. The latter distinction is critical in monitoring the treatment of cancer by radiation and chemotherapy, since it is well-established that hypoxic regions are three or four times more resistant to treatment compared to normoxic regions. The aim of this article is to describe pO_2 maps based on the *intrinsic* resolution of EPRI. A spectral parameter that affects the intrinsic spatial resolution of EPRI is the full width at half maximum (FWHM) height of the gradient-free EPR absorption line in frequency-encoded imaging. In single point imaging too, the transverse relaxation times (T_2^*) limit the resolution since the signal decays by $\exp(-t_p/T_2^*)$ where the delay time after excitation pulse, t_p, is related to the resolution. Although the spin densities of two point objects may be resolved at this separation, it is inadequate to evaluate quantitative changes of pO_2 levels since the linewidths are proportionately affected by pO_2. A spatial separation of at least twice this resolution is necessary to correctly identify a change in pO_2 level. In addition, the pO_2 values are blurred by uncertainties arising from spectral dimensions. Blurring due to noise and low resolution modulates the pO_2 levels at the boundaries of hypoxic and normoxic regions resulting in higher apparent pO_2 levels in hypoxic regions. Therefore, specification of intrinsic resolution and pO_2 uncertainties are necessary to interpret digitally processed pO_2 illustrations.

Published by Elsevier Inc.

1. Introduction

Precise monitoring of tissue oxygen status is important in managing cancer, since hypoxic regions (pO_2 < 10 mm of Hg) are three to four times more resistant to radiation and chemotherapeutic treatments than the tissues at normoxia [1–3]. Imaging modalities used to probe tissue oxygenation have specific spatial resolution capabilities based upon measurement parameters, instrument-dependent artifacts and, additionally temporal resolution, especially in studies involving an externally infused imaging probe (e.g., EPR, and PET) under the pharmacokinetic control of a living system [4,5]. While it is straightforward to ascertain the typical image resolution of a given imaging technique, due to probe characteristics or instrument parameters used in a particular procedure, it is difficult to interpret the actual resolution in a quantitative manner. An example would be to determine the spatial resolution of pO_2 derived from the EPR line width of a paramagnetic spin probe, whose line width itself depends on pO_2 in a given location. In other words, hypoxic locations are better spatially resolved than normoxic locations! The pO_2 values are derived from the pixel-wise decay of intensities from a set of T_2^*-weighted multi gradient, multi delay images [17]. Pixels with more oxygen have a shorter T_2^* and hence the SNR of these pixels suffer at large delays leading to some uncertainties in pO_2 arising from such an increased noise. The relatively less oxygenated regions, on the other hand, show better SNR even at large delays from the pulse. For the spin distribution image we can always select one with intermediate time delay, and therefore spin images are always better resolved than oxygen images. In addition, uncertainties in pO_2 values arising from random noise [6] become the limiting factors to distinguish pO_2 values of the objects that are spatially better resolved.

* Corresponding author. Address: Biophysical Spectroscopy, Radiation Biology Branch, CCR, NCI, National Institutes of Health, Bethesda, MD 20892, USA. Fax: +1 301 480 2238.
E-mail address: murali@helix.nih.gov (M.C. Krishna).
[1] These authors contributed equally to this work.

In multimodality imaging, where different aspects are derived from different complimentary imaging methods (e.g., EPRI and MRI), co-registration of images with very different resolution characteristics may be required. These co-registration efforts may help to enhance the interpretation of the low-resolution image based on details derived from the better resolved complementary image. For example, co-registration of anatomical MR images having high spatial resolution can provide a much better localization of hypoxic zones in a tumor derived from much less resolved EPR oxygen images. In this article, we examine the topic of resolution (reported in many publications simply based on theoretically derived values, often confusing the digital resolution with intrinsic resolution) [7] in a multimodality co-registration approach. We explore various aspects such as how the image quality depends on digital resolution, intrinsic resolution, the line shape function, relative intensities from adjacent locations, and convolution with point spread function. Based on our observations, we suggest a modified way of presenting the actual image resolution information in addition to the usual gray or color scale. The advantage of co-registration of a poorly resolved functional image and a highly resolved complimentary anatomical image in a multimodality imaging setting is also outlined with particular reference to EPR and MR images in mouse tumor studies.

2. Methods

2.1. Animal preparation

Six to eight week old female C3H mice weighing about 25 g were used for in vivo EPR and MR imaging. The animals (Frederick Cancer Research Center, Animal Production, Frederick, MD) were housed in a climate controlled room and fed ad libitum. Tumor (SCCVII) cells were injected subcutaneously as a single suspension of 10^6 cells in the right hind leg. Tumors grew to 1.5 cm diameter ($\sim$1.8 cm^3 in volume) in approximately 10 days. All in vivo experiments were carried out in compliance with the Guide for the care and use of laboratory animal resources (National Research Council, 1996) and approved by the National Cancer Institute Animal Care and Use Committee.

Mice were anesthetized by isoflurane (1.5%) inhalation and mounted prone with hip positioned downwards on a home built transmit–receive resonator coil. Breathing rate (60 ± 10 per min) was monitored by a pressure transducer (SA Instruments, Inc., NY). Core body temperature was maintained at 37 ± 1 °C by a steady flow of warm air. A 30 gauge needle was cannulated into the tail vein and extended using an optimum length of polythene tubing to administer Oxo-63 spin probe (Nycomed Innovation AB, Malmo, Sweden).

2.2. Phantom preparation

A cylindrical resolution phantom made of Lucite with cylindrical and a gradation of rectangular partitions with the minimum slot width of 300 μ filled with 3 mM Oxo-63 solution was used for EPRI measurements to demonstrate the effect of digital enhancement. This phantom was placed inside the resonator and carefully aligned such that a 2D transverse image (a plane perpendicular to the cylinder axis) will show circular and rectangular slots of spin distribution, the smallest spin filled slot and separation between filled slots being 300 μ (Fig. 1).

2.3. Imaging

MRI studies were performed using a 7T horizontal scanner operating on a Paravision platform (Bruker BioSpin Corporation, Billerica, MA). The transmit/receive resonator coil including the
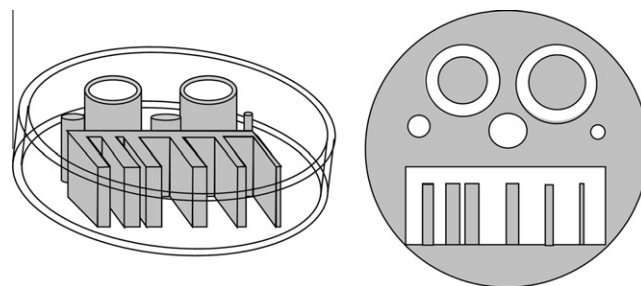

Fig. 1. Schematic of a resolution phantom consisting of a hollow Lucite cylinder with rods, tubes and rectangular slabs positioned inside (shaded regions) such that when filled with a spin probe, transverse 2D view perpendicular to the cylinder axis appears as on right with shaded portions being filled with the spin probe and the white portions being spin-free.

animal in the holder was transferred to MRI scanner after EPR imaging to ensure identical orientation. Fast spin echo images of the tumor leg were acquired with 14 contiguous slices using RARE (TE/TR = 13/2500 ms, RARE factor = 8), in plane resolution = 109 μm, slice thickness = 2 mm, FOV = 28 × 28 mm.

EPR images were acquired using single point imaging on a home made FT-EPR imager operating at 300 MHz and maximum gradients of 8, 10 and 12 mT/m involving three inter-leaved measurements. Spatial encoding is done using phase encoding in all directions. Since slice selection is not feasible in EPR, volume 3D images, and projected 2D images were measured. Impulse responses in terms of FIDs in presence of gradients which are looped in two or three dimensions with 21–31 gradient steps in each direction were collected. For each gradient setting about 4000 FIDs were summed for signal averaging. Instrument background subtraction was achieved by collecting the data in the absence of magnetic field under identical conditions and subtracting the same from the signals. Quadrature detection was employed using CYCLOPS phase cycling. K-space data were generated from the FIDs by looking at the modulation of a given time point by the gradient raster which generates a pseudo echo similar to gradient recalled echo imaging modality in MRI. Images were reconstructed by 2 and 3-dimensional Fourier transform after suitable zero-filling depending on the required digital resolution enhancement. Oximetry was carried out by choosing a sequence of time-delays and the resulting images were interpolated to identical FOV followed by evaluating the pixel-wise decay constant (T_2^*) using a least squares fitting, assuming a single exponential decay. The decay constant T_2^* are related to the oxygen dependent line width. Calibration of oxygen relaxivity is done using standard oxygen equilibrated solutions. Full details of oximetry based on SPI have been previously published [8]. The SNR of EPR images vary within an image considerably. The areas with maximum spin perfusion has a contrast to background ratio of $\sim$50 and that of poorly perfused areas are below 10. Those areas which are below 5% of maximum intensity in spin concentration are removed from oximetric analysis by suitable thresholding.

Reconstruction of EPR images and coregistration with MRI were done using scripts developed in MATLAB (The Mathworks Inc., Natick, MA). All slices from MRI and 3D EPR image were used for co-registration and an MRI slice showing the middle portion of the tumor-bearing leg containing a large hypoxic core surrounded by more oxygenated peripheral tissues was selected for presentation. A corresponding EPRI slice was calculated at matched digital resolution by interpolations and summations as required.

3. Results and discussion

The resolution (R) specifies the finest division of a continuous scale that can distinguish two points without ambiguity, and is

limited by the precision at which quantities represented by the scale (e.g. of image intensities) can be estimated. For spectral lines, the resolving power is given by the Rayleigh criterion (the accepted criterion for minimum resolvable detail) is said to be diffraction limited and is defined as the separation between two lines where the peak of one line occurs at the first minimum of the other [9]. For EPR imaging, the spatial resolution is given in terms of full width at half maximum (FWHM, Δ) of a Lorentzian line shape [10]. For digital images, the resolution is specified by the number of divisions (n) per unit length where n is a quantity equals to 1/R. We refer to "high resolution" for larger n or smaller R indicating the ability to examine the image in higher detail. At low resolution, the object size artificially appears to be bigger than actual size due to large pixel size (Fig. 2). At higher resolutions, finer details of the image are revealed with more accurate object boundaries.

3.1. Effect of digital enhancement on low resolution

The intrinsic resolution of an image is limited by the factors inherent to the technique. In SPI, gradient strength and transverse relaxation times (T_2^*) limit the resolution since the signal decays by $\exp(-t_p/T_2^*)$ where the delay time after excitation pulse, t_p, and gradient magnitude are related to the obtainable resolution. In CW spatial imaging, the gradient strength to linewidth ratio is a parameter that limits the intrinsic resolution. Elimination of an inherent factor e.g. by deconvolution of gradient free line shape from raw data may enhance the resolution but is subjected to the accuracy of such algorithm. Knowledge of intrinsic resolution is particularly helpful in interpreting the resolution enhanced images, as for example images at higher digital resolution can be produced from the low resolution images by mathematical treatments. Digital enhancement may be achieved by prediction of pixel intensities using interpolation methods such as linear, cubic, spline or zero-filled Fourier transform (FT) techniques. Here we have used the Fourier/sinc interpolation kernel. Irrespective of the interpolation technique used, enhancement of digital resolution beyond the intrinsic resolution does not improve the image quality *per se*, other than rounding of sharp corners or diffusing any abrupt contrast. FT-EPR image of a phantom reconstructed from k-space data at intrinsic resolution (FOV = 25.9 mm, n = 61 and a resolution of 0.42 mm/pixel) and at higher digital resolutions (n = 128, and 256 with 0.2 and 0.1 mm/pixel) are shown in Fig. 3. The window-level in these images was adjusted to emphasize edge contrast. The 2D view of the phantom appears as a circular disk containing two large open circles at the top, three smaller filled circles below them and a comb-like shape. The comb-shape has teeth of different widths and different gap widths between the teeth (Fig. 3). In the images at n = 128 and 256, the open and closed circles appear to have much smoother edges than at n = 61 (the intrinsic resolution). The improved detail of these digitally enhanced images may not necessarily mean an increase in resolution since it depends on the algorithm used for enhancement. Fourier interpolation at a larger matrix size does not improve the intrinsic resolution of the technique since the image space is calculated at
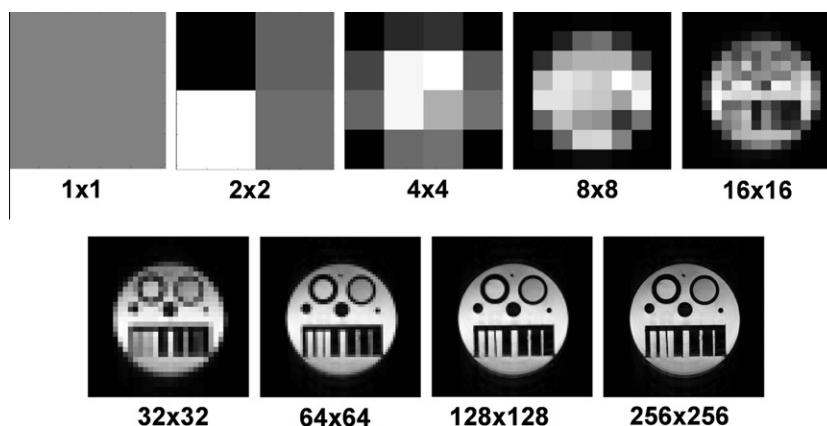

Fig. 2. The image of the phantom in Fig. 1 at different resolutions. A slice of MR image at size 256 × 256 was used to calculate the low-resolution images. The object size appears to be artificially larger at low resolution.
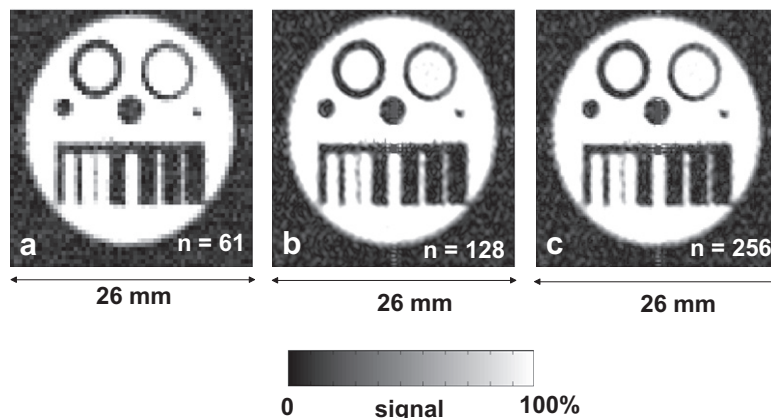

Fig. 3. Digital enhancement of a low resolution image. A 2D spin density image of the phantom filled with Oxo-63 spin label. Images were reconstructed at digital resolutions: (a) at intrinsic resolution (n = 61), (b) reconstructed at image size of 128 × 128, and (c) reconstructed at image size 256 × 256. The circular shapes appear better in (c) than in (a) though the intrinsic resolution is the *same* for all the three images.

the same k-space resolution. The digital enhancement in Fig. 3 is just a smoothening effect of interpolation, as can be seen in the noise (non-signal containing) regions of the images.

3.2. Combining images of two different resolutions for co-registration

Digital enhancement and emulation of pixel intensities are unavoidable while co-registering two images having very different intrinsic resolutions. As an example, we show a comparison of the phantom image obtained by proton MRI at high resolution with spin density EPR images obtained at three lower spatial resolutions (Fig. 4). The top row in Fig. 4 shows the images at their intrinsic resolution in which each square represents a pixel and the spin density is indicated by its brightness. The area covered by each pixel increases at lower resolution which results in blurring of the image. The open and closed circles are clearly visible at MRI resolution ($R = 0.125$ mm/pixel, $n = 204$) while the EPR images scanned at $R = 0.42$, 1.21 and 1.42 mm/pixel ($n = 61$, 23 and 21 respectively) have diffuse edges. At $R = 0.42$, the larger circular shapes including two open and two filled circles on left are apparent, but the small filled circle at right appears as a square. At $R = 1.21$ and 1.42, the bigger closed circle on the left also appears as a square and the center of the open circle is blurred. The intensity profile of a row in the comb like region depicts the resolvable gaps between filled regions. In the image, the narrowest gap is the third line from left and the most narrow fill is the first bright line from the right. These are clearly visible at MRI resolution. Both are well defined with a slight blur in EPR image at $R = 0.42$ mm, but are totally blurred at $R = 1.21$ and 1.42 mm. The pixel intensity line graph of a row in the comb-like regions is shown below these images in Fig. 4. At high resolution a sharp change of signal between maximum and minimum values depending on the presence and absence of spin probe respectively is observed. As the resolution is decreased, the profiles become broader indicating blurring of the image.

A comparison of downsizing of higher resolution images is shown in middle row of Fig. 4. These images were computed by summing the pixel intensities by laying out spatial grid equal to the image at smallest intrinsic resolution ($R = 1.42$ mm). Reducing matrix size to 21 leads to smearing of intensities of neighboring pixels but the circular shapes still appear better at high intrinsic resolution. All the four images reconstructed at a digital resolution
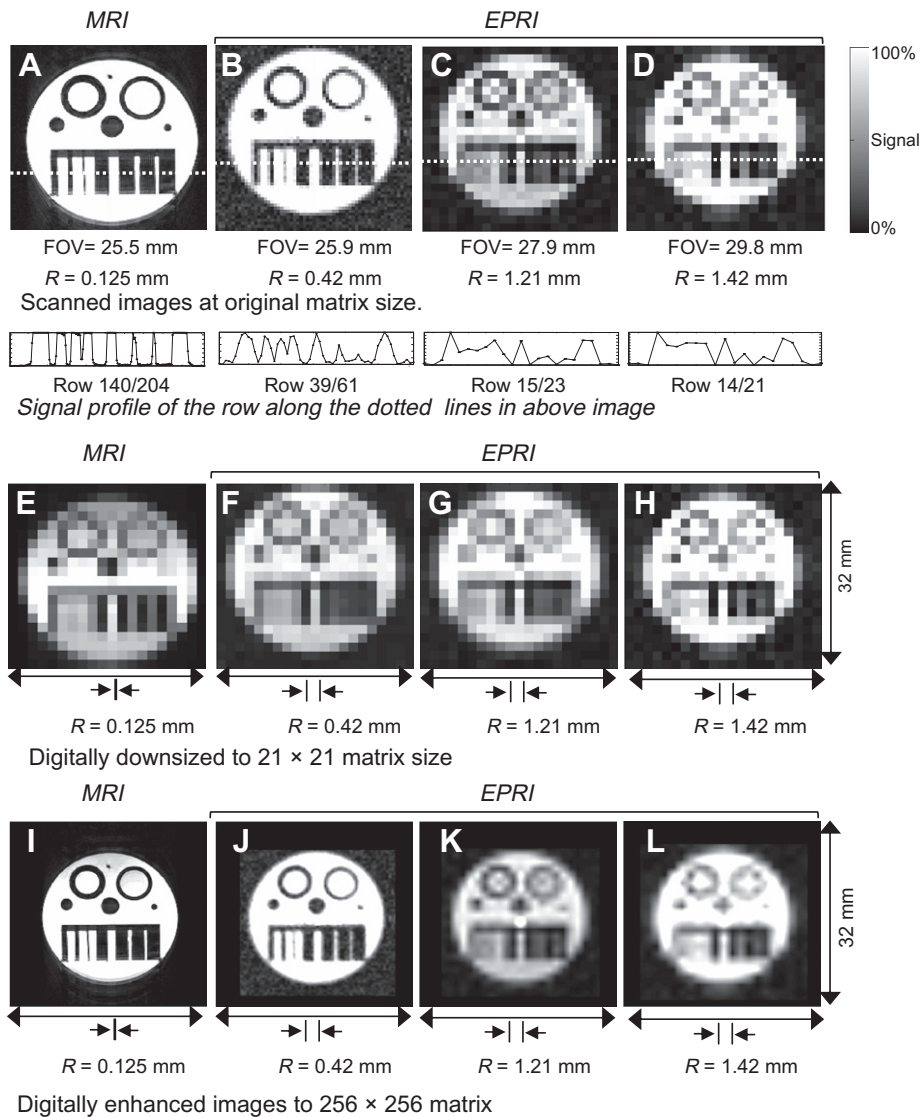

Fig. 4. Comparison of intrinsic resolution with digital enhancement of a 2D spin density image of a phantom filled with Oxo-63 spin label. (A) MRI scanned at 0.125 mm resolution. (B), (C), and (D) are EPR images scanned at the intrinsic resolutions of 0.42, 1.21 and 1.42 mm respectively. The horizontal gray lines in image indicate a row selected for signal intensity profile shown below the image. (E–H): Down sized images of (A–C) to match with matrix size of (D). (I–L): The images (A–D) reconstructed at $n = 256$ for coregistration. Note the blur in EPR images (G) and (H) because of low intrinsic resolution in spite of equal digital resolution with (F).
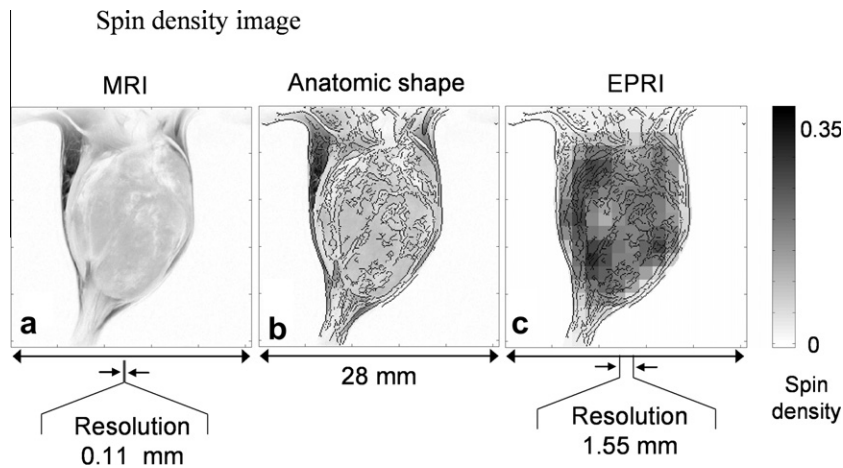
Fig. 5. Coregistration of EPR spin density image with MR anatomic image of a tumor bearing mouse hind leg. (a) MRI at resolution 0.109 mm. (b) Solid lines drawn at the intensity gradients trace the anatomic shape. (c) EPR image at its intrinsic resolution of 1.55 mm and overlay of the edges from MRI. High resolution MRI lends support to low resolution EPRI to delineate anatomic locations. Data are from a slice of 3D image.

equal to MRI are shown in the bottom row of Fig. 4. The circular shapes in EPR images are defined better in these illustrations than before; however, the edges still remain blurred. Comparison of the image at $R = 0.125$ mm to $R = 1.42$ mm clearly points out that the anatomical shapes are not resolved any better by this mere digital enhancement.

A comparison of anatomic MR image and spin density EPR image of hind leg of a tumor bearing mouse is shown in Fig. 5. The intrinsic resolutions of MR and EPR images are 0.109 and 1.55 mm, respectively. The MRI and EPRI modalities, besides having very different resolutions (MRI being of a much higher resolution), capture very different aspects in their images. MRI deals with water distribution inside the animal and the proton density images that are obtained often provide nearly full anatomic details with local viscosities and dynamics providing characteristic contrasts. EPRI, on the other hand just captures the distribution of the unpaired spin and often areas with very low or negligible spin perfusion will not show up and as such the anatomical details are much less defined. The contrast in EPR images comes both from distribution of the spin by perfusion and the relaxivity of *in vivo* oxygen.

The oval shape of the tumor is apparent in MRI (Fig. 5a) while EPR spin density image (Fig. 5c) appears to be diffuse. In spite of the low resolution of the EPR image, co-registration can be done almost at the precision of MR image by matching distantly located land marks (fiducials). The overlay of the edges from MRI on EPR image (Fig. 5c) indicates that the spin probe density around the tumor region is higher than inside the tumor. The co-registration demonstrates the differences of spin probe and water distributions inside tumor leg.

3.3. Understanding pO$_2$ maps

Quantitative interpretation of pO$_2$ map is important to delineate hypoxic and normoxic regions, and to evaluate oxygen levels during perfusion experiments. A pO$_2$ image slice of a tumor bearing mouse obtained by EPRI is shown in Fig. 6. The image was digitally converted from a $19 \times 19 \times 19$ matrix into $256 \times 256 \times 14$ matrix for co-registration with MR image. A characteristic feature of digital enhancement is smoother gradients of pO$_2$ levels (Fig. 6c). The smearing of region boundaries due to low resolution and blurring is obscured by apparent higher digital resolution, and this will be a general feature with similar trends irrespective of the exact nature of the interpolation kernel used.

3.3.1. Spatial resolution

The resolution of pO$_2$ map depends on (i) spatial resolution of spin densities and (ii) spectral parameters to estimate pO$_2$ values. Both of these depend on spectral line width of the spin probe. The effect of gradient strength relative to EPR line widths [11], signal to noise characteristics [10], and sampling of data on spatial resolution of EPR images are well documented in literature [12,13]. In general, the spatial resolution of EPR images is improved by higher gradient strengths, better SNR and sensitivity of the imager, smaller line widths of spin probes and higher data sampling rate for image reconstruction. While small line widths achieve high spatial resolution, the presence of pO$_2$ increases the line width and thereby reducing the spatial resolution. The local variations of pO$_2$ levels influence line widths causing local variations in spatial resolution. For Oxo-63 spin probe, the line width may increase by 33% from hypoxia to a local pO$_2$ of 5% [14].

If two objects are spatially unresolved in an image, their signals overlap with each other and the pO$_2$ values of both objects are smeared. Consider a 1D space of spin densities divided into equal size pixels. Pixels separated by Δ (FWHM) would get about 12% of each neighboring pixel's intensity for a Gaussian shape and 15% for a Lorentzian shape. However, this overlap becomes negligible for Gaussian (1%) at a pixel width of 2Δ. Although, the Lorentzian overlaps are considerable even at a pixel width of 4Δ (5%), background correction grossly removes their effect [15].

Gaussian overlaps of a hypothetical 1D image having five equally spaced point objects of spin densities of 6, 6, 6, 1, 1 at separations of Δ and 2Δ are shown in Fig. 7a and b. The traces shown in thin lines indicate signals from individual objects and their summation shown by thick line represents observed signal. The vertical grid lines are pixel boundaries. The pixel intensities calculated from Fig. 7a are 5.28, 6, 5.4, 1.6, 0.88 and from Fig. 7b are 5.94, 6, 5.95, 1.05, 0.99. Note that the 4th object has intensity 1.6 instead of its original value of 1 when $R = 1/\Delta$. The effect of overlaps on neighbors is greater when a low spin density is next to a high spin density. But the errors due to overlaps are reduced by an order of magnitude at $R = 1/2\Delta$ (Fig. 7b).

In SPI mode, the pixel-wise signal decay of the sequence of T_2^*-weighted images considered for oximetry, is governed by $\exp(-t_p/T_2^*)$ where T_2^* is inversely related to pO$_2$. An example of signal decay for arbitrary linewidths of Δ, 1.5Δ and 2Δ to represent oxygen free and two different pO$_2$ levels is shown in Fig. 7d. The horizontal line drawn at a hypothetical SNR of 1% of maximum
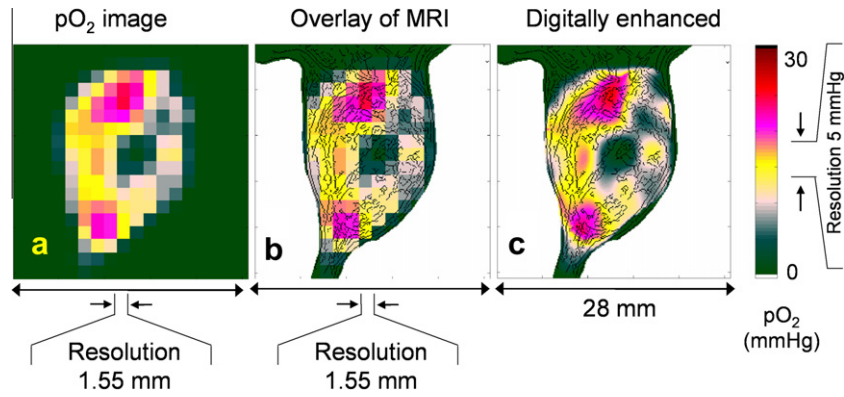
Fig. 6. Resolution indication on the image. (a) pO$_2$ map at intrinsic resolution of 1.55 mm. (b) Overlay of the anatomic shape from MRI. (c) Digitally enhanced to match to MRI size of 256 × 256. The spatial resolution is shown on spatial dimension. The uncertainty level of pO$_2$ is shown on pO$_2$ scale.
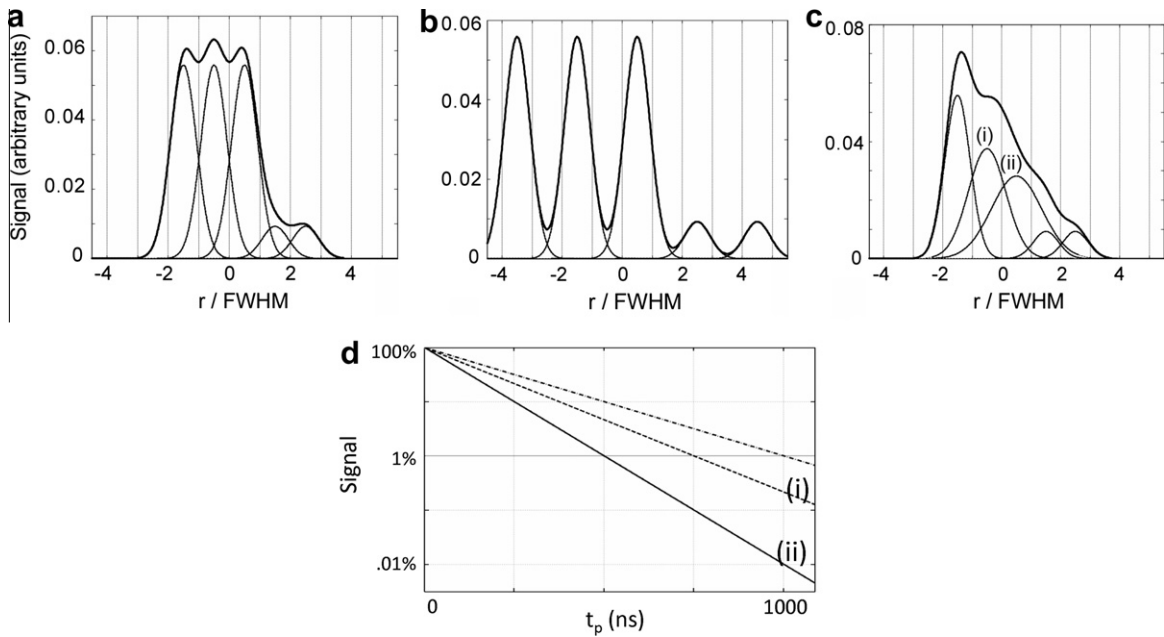

Fig. 7. Simulation of signals using hypothetical point objects having spin densities of 6, 6, 6, 1, 1. The objects are equally spaced. (a) Spacing = Δ. Grid lines indicate the pixels boundaries at this spacing. (b) Spacing = 2Δ. (c) Effect of line width variation on (a). The line widths of objects (i) and (ii) are 1.5Δ and 2Δ respectively. Line width increase due to pO$_2$ leads to higher overlaps. (d) Signal decay with time in SPI for hypothetical T_2 values. Relative signal levels with time are shown at T_2 values representing the line widths of Δ, 1.5Δ (i) and 2Δ (ii) respectively. The horizontal line at 1% of the signal intersecting the decay curves at different t_p values indicates the limits available for SPI at a hypothetical SNR level. SPI resolutions available for pO$_2$ mapping are lower than oxygen free conditions because of reduced t_p limits.
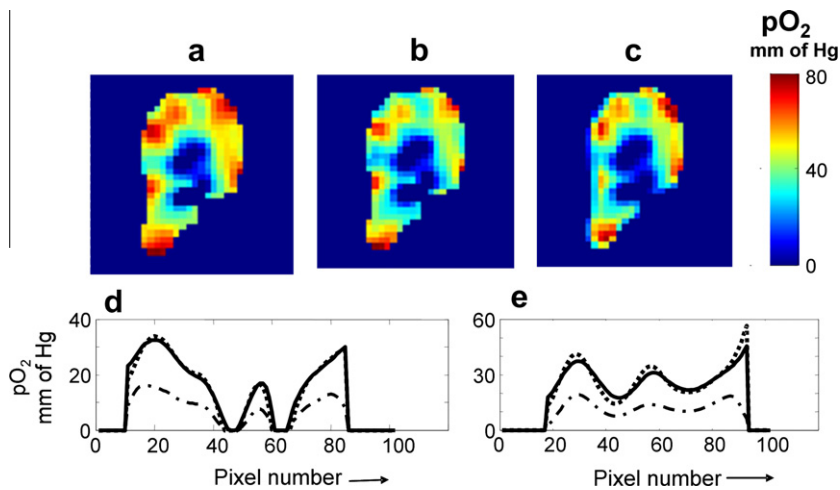

Fig. 10. pO$_2$ map of a slice from 3D EPR image of a tumor bearing mouse leg at the intrinsic resolution of 1.55 mm. (a) Before deconvolution. (b) pO$_2$ map calculated using spin densities after deconvolution as shown in Fig. 9b. (c) pO$_2$ map obtained by the deconvolution of the one derived from raw images (Fig. 9a).
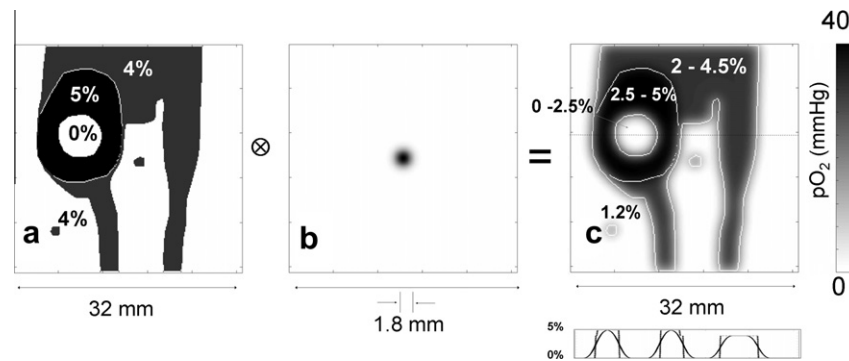
Fig. 8. (a) A hypothetical pO$_2$ image schematically representing tumor (left) with hypoxic core (0%), surrounding high oxygen region (5%) and normoxic regions (4%). The two dots represent fiducials. The thin white lines indicate boundaries of pO$_2$ regions. (b) The point spread function (Gaussian noise) (c) convolution of (a) and (b). The blurring leads to distorted pO$_2$ values at the region boundaries. Note that the fiducials that are at normoxic levels are highly diffused by noise to almost hypoxic levels. At region boundaries hypoxic regions appear to have higher pO$_2$ values (0–2.5%) while normoxic regions appear to be at lower pO$_2$ levels (2–4%). pO$_2$ profile across the tumor indicated by dashed line is shown below (c). Blurred image profile appears as a curve tracking pO$_2$ levels before blurring.
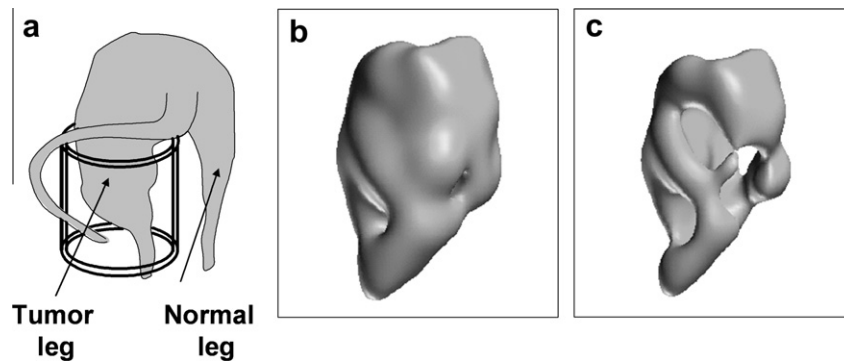

Fig. 9. Spin density 3D EPR image of a tumor bearing mouse leg. (a) The positioning of the tumor-bearing leg on a 17 mm resonator. Surface-rendered images at identical angles and cut-off intensity (b) before and (c) after deconvolution.

signal level intersects the curves of faster decays at smaller t_p values compared to decay for linewidth of Δ. Because of this decrease in the presence of oxygen, it is necessary to use a t_p value smaller than that is suitable to oxygen free conditions for imaging both normoxic and hypoxic regions. Ignoring this condition leads to artifacts caused by lack of detection of high pO$_2$ regions that fall within noise level.

3.3.2. Probe characteristics

Each spin probe has characteristic: (1) pO$_2$ range that can be covered (2) sensitivity of spin probe to O$_2$ and (3) specificity.

The sensitivity of the spin probe is proportional to the magnitude of line broadening caused by O$_2$. The line width variation of a narrow EPR line is relatively a smaller quantity than the peak height variation. In practice, the line widths and their uncertainties are estimated by fitting all the data covering entire line shape. The line width uncertainties are determined from the residuals of the fit. Therefore the precision of pO$_2$ depends on both the sensitivity of the probe to O$_2$ and SNR. While high oxygen sensitivity of probe is advantageous to measure low pO$_2$ levels at better precision, it is disadvantageous to measure high oxygen levels since the line broadening decreases the spatial resolution and SNR. The spin probes sensitive to low pO$_2$ levels are good enough for biomedical applications to delineate hypoxic and normoxic regions which deal with limited pO$_2$ range (0–76 mm Hg).

The line widths are also affected by spin probe concentration, viscosity, temperature and instrument settings. The contributions to line width from the factors other than O$_2$ have to be compensated for accurate determination of pO$_2$ values. Conventionally,

pO$_2$ values are calculated from observed line widths using calibration data generated in non-imaging experiments. The specificity of pO$_2$ values depends on the accuracy of line width in the absence of oxygen and the proportionality constant between pO$_2$ and linewidth. Inaccurate estimate of natural line width adds or subtracts a constant amount of pO$_2$ value to the entire image leading to under or over estimation of hypoxic regions. Inaccurate proportionality constant leads to relative pO$_2$ estimates instead of absolute quantities. It is important to fine tune the calibration data from non-imaging experiments to imaging conditions. The calibrations determined by *in vitro* measurements often require corrections to account for local concentration, viscosity and temperature variations of *in vivo* studies.

3.4. Blurring

Every point in the measured spin density image is essentially an EPR line characterized by a shape and height. When the line shape is constant, the observed image can be described by a convolution of spin densities with line shape function [16]. Assessment of oxygen levels from the line shape are associated with uncertainties arising from noise characteristic to the technique including motion effects, gradient imperfections and random noise. Both the intrinsic resolution specified by spectral line width and gradient strengths, and other sources of noise contribute to the point spread function of the pO$_2$ image. Supposing that observed and true images are O and I respectively and P is a point spread function (PSF), the intensity of O at point z is expressed by convolution as

$$O(z) = \int I(x)P(z - x)dx \text{ or}$$
$$O = I \otimes P \tag{1}$$

where $\otimes$ represents convolution. When EPR line shape (P) is known, the true spin densities I can be recovered from observed image O by deconvolution. The effect of a Gaussian PSF on a hypothetical pO_2 map is shown in Fig. 8. This image depicts tumor bearing and normal hind legs of a mouse and two fiducials placed in between and at the side of the legs. The pO_2 regions of tumor include hypoxic core surrounded by high oxygen layer, while the remaining including fiducials exhibit normoxic levels. When P is a Gaussian PSF (Fig. 8b) the hypothetical pO_2 is blurred (Fig. 8c). The hypoxic regions with higher pO_2 values are smeared with lower pO_2 values at normoxic regions at the boundaries. We see that the hypoxic core becomes smaller and the oxygen rich layer surrounding the tumor becomes narrow by diffusing both into normoxic and hypoxic regions. Additionally, the fiducial diameter increases, and its pO_2 level falls close to hypoxic values.

Deconvolution [10,16–19] of a pO_2 map to remove this blurring is often complicated because line widths vary with changes in oxygen level. Deconvolution of approximate PSF's including contributions of the natural EPR line shape and random noise can partially sharpen the image. In the single point imaging (SPI) technique, k-space sampling interval is determined as a function of t_p which is proportional to the image field of view and thus intrinsic resolution. In other words, a series of images at different resolutions are naturally obtained in SPI.

Considering that a low resolution image is a convolution of high resolution image and a PSF, one can estimate PSF to use with deconvolution within a single SPI dataset. We have estimated PSF by this procedure and found that it is approximately Gaussian. The deconvolution of spin density image by this procedure is shown in Fig. 9. The deconvolution clearly shows sharpening of the object dimensions similar to the original object proposed in Fig. 7a. The pO_2 calculation using these spin densities leads to a sharpened pO_2 map where the hypoxic core appears to be much larger as expected. However, deconvolution does not necessarily improve resolution. When the PSF is estimated within a set of SPI images, the images are similarly sharpened, except in this case the linewidths are uniformly scaled down by a factor in proportion to the ones obtained from un-deconvolved images, without affecting, however, the spatially resolved relaxivity information. These are summarized in Fig. 10 (shown below Fig. 7).

3.5. Indication of intrinsic resolution

The data presentation as an image can be a limiting factor in some situations. For example, the spatial resolution may be much higher than depicted in an illustration. At the other extreme, a computer can present the number of shades of colors or grays much higher than human eye can distinguish. For example, in Fig. 6b, only a few shades of pO_2 levels are spatially distinguishable by the eye though it contains 64 color shades. Therefore explicit indication of resolution of the scale as shown in Fig. 6 is helpful in interpreting pO_2 maps. The hypoxic core inside tumor region appears as a dark square and its surrounding regions at higher pO_2 levels appear bright at different levels (Fig. 6b and c). Co-registration with MRI facilitates the identification of anatomic locations in EPRI accurately both at its intrinsic resolution (Fig. 6b) and digital enhancement (Fig. 6c). An illustration of pO_2 map as in Fig. 6c without resolution indication exaggerates the precision at which the hypoxic regions can be outlined. This ambiguity is removed either by using illustrations at intrinsic resolution as in Fig. 6a and b or by explicit indication of resolution.

4. Summary

Digital enhancements are desirable in the current state of co-registration of multi modality imaging for comprehensive knowledge of physiology. Explicit indication of the intrinsic resolutions of individual modalities improves understanding of co-registrations intuitively, and these ought to be indicated along with the color or gray bar scales that are presented conventionally. A separation of 2Δ between the objects in EPR image is necessary to examine pO_2 difference. The regions separated by less than 2Δ are smeared by overlaps from neighbors. The noise and uncertainties lead to blurring of pO_2 values at boundaries of hypoxic and normoxic regions. Removal of noise and increasing intrinsic resolution are helpful in improved delineation of hypoxic and normoxic regions. Deconvolution helps in deblurring the images and helps remove the diffuse edges of images that present an apparent enlargement of dimensions. Caution has to be exercised in deriving quantitative oximetry from deconvolved images and a pre-calibration with standards subjected to identical deconvolution procedure can improve the reliability of pO_2 values.

References

[1] M. Hockel, K. Schlenger, B. Aral, M. Mitze, U. Schaffer, P. Vaupel, Association between tumor hypoxia and malignant progression in advanced cancer of the uterine cervix, Cancer Res. 56 (1996) 4509–4515.

[2] M. Hockel, P. Vaupel, Tumor hypoxia: definitions and current clinical, biologic, and molecular aspects, J. Natl. Cancer Inst. 93 (2001) 266–276.

[3] J.M. Brown, Tumor hypoxia, drug-resistance, and metastases, J. Natl. Cancer Inst. 82 (1990) 338–339.

[4] R.S. Liu, T.K. Chou, C.H. Chang, C.Y. Wu, C.W. Chang, T.J. Chang, S.J. Wang, W.J. Lin, H.E. Wang, Biodistribution, pharmacokinetics and PET imaging of [(18)F]FMISO, [(18)F] FDG and [(18)F]FAc in a sarcoma- and inflammation-bearing mouse model, Nucl. Med. Biol. 36 (2009) 305–312.

[5] K. Matsumoto, S. English, J. Yoo, K. Yamada, N. Devasahayam, J.A. Cook, J.B. Mitchell, S. Subramanian, M.C. Krishna, Pharmacokinetics of a triarylmethyl-type paramagnetic spin probe used in EPR oximetry, Magn. Reson. Med. 52 (2004) 885–892.

[6] S. Subramanian, K. Yamada, A. Irie, R. Murugesan, J.A. Cook, N. Devasahayam, G.M. Van Dam, J.B. Mitchell, M.C. Krishna, Noninvasive in vivo oximetric imaging by radiofrequency FT EPR, Magn. Reson. Med. 47 (2002) 1001–1008.

[7] M. Elas, B.B. Williams, A. Parasca, C. Mialer, C.A. Pelizzari, M.A. Lewis, J.N. River, G.S. Karczmar, E.D. Barth, H.J. Halpern, Quantitative tumor oximetric images from 4D electron paramagnetic resonance imaging (EPRI): methodology and comparison with blood oxygen level-dependent (BOLD) MRI, Magn. Reson. Med. 49 (2003) 682–691.

[8] N. Devasahayam, S. Subramanian, R. Murugesan, F. Hyodo, K.I. Matsumoto, J.B. Mitchell, M.C. Krishna, Strategies for improved temporal and spectral resolution in in vivo oximetric imaging using time-domain EPR, Magn. Reson. Med. 57 (2007) 776–783.

[9] F.A. Jenkins, H.E. White, Fundamentals of Optics, Mc_Graw-Hill, New York, 1957.

[10] G.R. Eaton, S.E. Eaton, K. Ohno (Eds.), EPR Imaging and in vivo EPR, CRC Press, Boca Raton, 1991.

[11] P. Mansfield, P.G. Morris (Eds.), NMR Imaging in Biomedicine, vol. Suppl. 2, Academic Press, New York, 1982, pp. 1–343.

[12] R.A. Brooks, G.D. Chiro, Principles of CAT in radiographic and radioisotopic imaging, Phys. Med. Biol. 21 (1976) 689–732.

[13] U. Ewert, T. Herrling, Numerical analysis in electron paramagnetic resonance zeugmatography with modulated gradient, J. Magn. Reson. 61 (1985) 11–21.

[14] K.I. Matsumoto, S. Subramanian, R. Murugesan, J.B. Mitchell, M.C. Krishna, Spatially resolved biologic information from in vivo EPRI, OMRI, and MRI, Antioxid. Redox Signaling 9 (2007) 1125–1141.

[15] L.E. Creasy, A critical evaluation of line overlap corrections in X-ray spectroscopy, Adv. X-ray Anal. 44 (2001) 361–367.

[16] A.R. Stokes, A numerical Fourier-analysis method for the correction of widths and shapes of lines on X-ray powder photographs, Proc. Phys. Soc. (London) 61 (1948) 382–391.

[17] L.C. Allen, S.H. Glarum, H.M. Gladney, Resolution enhancement for spectra of chemical + physical interest, J. Chem. Phys. 40 (1964) 3135–3141.

[18] U. Ewert, R.H. Crepeau, C.R. Dunnam, D.J. Xu, S.Y. Lee, J.H. Freed, Fourier-transform electron-spin-resonance imaging, Chem. Phys. Lett. 184 (1991) 25–33.

[19] A. Sotgiu, D. Gazzillo, F. Momo, Electron-spin-resonance imaging – spatial deconvolution in the presence of an asymmetric hyperfine-structure, J. Phys. C Solid State 20 (1987) 6297–6304.